ALMA Observations of Giant Molecular Clouds in M33. II. Triggered High-mass Star Formation by Multiple Gas Colliding Events at the NGC 604 Complex

Kazuyuki Muraoka[1] , Hiroshi Kondo[1], Kazuki Tokuda[1,2] , Atsushi Nishimura[1] , Rie E. Miura[2] , Sachiko Onodera[3],
Nario Kuno[4,5] , Sarolta Zahorecz[1,2] , Kisetsu Tsuge[6] , Hidetoshi Sano[2] , Shinji Fujita[1] , Toshikazu Onishi[1] ,
Kazuya Saigo[2] , Kengo Tachihara[6] , Yasuo Fukui[6,7], and Akiko Kawamura[2]

[1] Department of Physical Science, Graduate School of Science, Osaka Prefecture University, 1-1 Gakuen-cho, Naka-ku, Sakai, Osaka 599-8531, Japan
kmuraoka@p.s.osakafu-u.ac.jp

[2] National Astronomical Observatory of Japan, National Institutes of Natural Science, 2-21-1 Osawa, Mitaka, Tokyo 181-8588, Japan

[3] Meisei University, 2-1-1 Hodokubo, Hino, Tokyo 191-0042, Japan

[4] Department of Physics, Graduate School of Pure and Applied Sciences, University of Tsukuba, 1-1-1 Tennodai, Tsukuba, Ibaraki 305-8577, Japan

[5] Tomonaga Center for the History of the Universe, University of Tsukuba, Tsukuba, Ibaraki 305-8571, Japan

[6] Department of Physics, Nagoya University, Chikusa-ku, Nagoya 464-8602, Japan

[7] Institute for Advanced Research, Nagoya University, Furo-cho, Chikusa-ku, Nagoya 464-8601, Japan

Abstract

We present the results of ALMA observations in $^{12}CO(J = 2 - 1)$, $^{13}CO(J = 2 - 1)$, and $C^{18}O(J = 2 - 1)$ lines and 1.3 mm continuum emission toward a massive ($\sim 10^6 \, M_\odot$) giant molecular cloud associated with the giant H II region NGC 604 in one of the nearest spiral galaxies, M33, at an angular resolution of $0.''44 \times 0.''27$ (1.8 pc $\times$ 1.1 pc). The ^{12}CO and ^{13}CO images show highly complicated molecular structures composed of a lot of filaments and shells whose lengths are 5–20 pc. We found three 1.3 mm continuum sources to be dense clumps at the edges of two shells and also at the intersection of several filaments. We examined the velocity structures of the $^{12}CO(J = 2 - 1)$ emission in the shells and filaments containing dense clumps, and concluded that expansion of the H II regions cannot explain the formation of such dense cores. Alternatively, we suggest that cloud–cloud collisions induced by an external H I gas flow and the galaxy's rotation compressed the molecular material into dense filaments/shells which are ongoing high-mass star formation sites. We propose that multiple gas converging/colliding events with a velocity of a few tens of kilometers per second are necessary to build up NGC 604, the most significant cluster-forming complex in the Local Group of galaxies.

Unified Astronomy Thesaurus concepts: Interstellar medium (847); Star formation (1569); Giant molecular clouds (653); Triangulum Galaxy (1712); Local Group (929); H II regions (694)

1. Introduction

Stars are formed by the contraction of the molecular interstellar medium (ISM), which can be initiated by spontaneous gravitational collapse or some triggering events, such as cloud–cloud collisions (converging flow), galactic shocks, and feedback from high-mass stars (e.g., McKee & Ostriker 2007; Dobbs & Baba 2014). In the past few decades, many observational studies toward the Local Group of galaxies (see the reviews by, e.g., Blitz et al. 2007; Fukui & Kawamura 2010; Heyer & Dame 2015) suggested that giant molecular clouds (GMCs) are major sites of high-mas star formation, and the formed stars eventually regulate the evolution of galaxies through their feedbacks such as radiation pressure, photoionization, and supernova explosions (Hopkins et al. 2012). Thus, the detailed study of GMC properties and the evolution of GMCs is one of the most important issues in modern astronomy.

Earlier molecular gas surveys using the CO molecule and its isotopes toward star-forming regions in the Milky Way (MW) revealed that filamentary structures are considered to be fundamental ingredients of molecular clouds (e.g., Mizuno et al. 1995; Onishi et al. 1996; Goldsmith et al. 2008; Hacar et al. 2013), and such filamentary molecular clouds eventually collapse into dense cores prior to star formation. In addition, high spatial resolution observations of molecular clouds outside the MW with the Atacama Large Millimeter/submillimeter Array (ALMA) are now providing new insights; recent ALMA

observations toward the Large Magellanic Cloud (LMC) suggest that the collision/interaction of the filamentary molecular clouds may drive the high-mass star formation. For example, Fukui et al. (2015) found that the CO distribution at a subparsec scale is highly elongated with a small width in the active star-forming region N159 West in the LMC. These elongated clouds (i.e., filaments) show a straight or curved shape with a typical width of 0.5–1.0 pc and a length of 5–10 pc. They also detected the molecular outflow toward the high-mass protostar located at the intersection of two spatially overlapping filaments, and thus they argued that the two filaments collided with each other and triggered the formation of high-mass stars (see also Saigo et al. 2017 for N159 East).

The role of galactic dynamics is also considered to be important for the onset of high-mass star formation. In the disks of spiral galaxies, molecular clouds and star-forming regions are preferentially distributed in spiral arms. This is because molecular gas can be accumulated in the potential minimum of stellar arms, and then the formation of dense molecular gas and high-mass stars are triggered due to galactic shock (Fujimoto 1968; Roberts 1969; Shu et al. 1973) caused by quasi-stationary density waves (e.g., Lin & Shu 1964) and/or cloud–cloud collisions. Thus, it is significant to investigate the relation between galactic-scale gas dynamics and the internal structure of GMCs for further understanding high-mass star formation.

The flocculent spiral galaxy M33 is one of the most preferable objects for this purpose. Its proximity ($\sim$840 kpc;
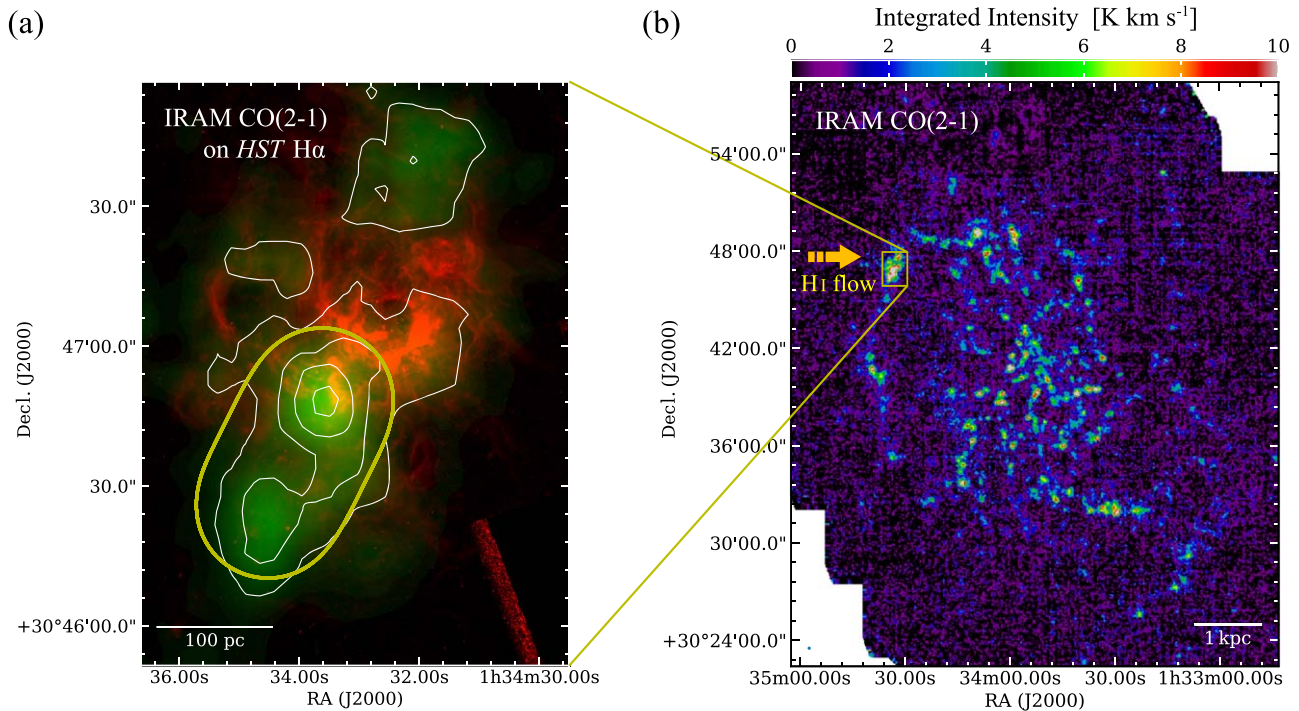
(a)

(b)

Figure 1. (a) Integrated intensity map in $^{12}CO(J = 2 - 1)$ emission of NGC 604 obtained by the IRAM 30 m telescope (white contour and green; Druard et al. 2014) superposed on the spatial distribution of Hα emission obtained with the Hubble Space Telescope (HST; red), which is available in the HST archive. The contour levels are 3, 6, 9, and 12 K km s^{-1}. The yellow line indicates the field of view of the ALMA observations. (b) Integrated intensity map in $^{12}CO(J = 2 - 1)$ emission of M33 obtained by the IRAM 30 m telescope (Druard et al. 2014). The angular resolution is shown in the lower left corner. The arrow indicates the infalling H I gas flow toward NGC 604 proposed by Tachihara et al. (2018; see Section 3.1).

Freedman et al. 2001) and favorable inclination (51°; Corbelli & Salucci 2000) enable us to resolve internal molecular structures of individual GMCs within the M33 disk by using ALMA. So far, a lot of observational studies on the ISM and star formation has been performed toward M33 (e.g., Engargiola et al. 2003; Heyer et al. 2004; Rosolowsky et al. 2007; Gratier et al. 2010; Onodera et al. 2010; Tosaki et al. 2011; Druard et al. 2014; Miura et al. 2014; Corbelli et al. 2017; Sano et al. 2021), and individual GMCs have been identified (Gratier et al. 2012; Miura et al. 2012; Corbelli et al. 2017). In particular, a massive (~$10^6 M_\odot$) GMC associated with NGC 604, which exists in the spiral arm (see Figure 1) and is the second most luminous supergiant H II region in the Local Group, after 30 Dor in the LMC, has been studied in various wavelengths; radio (Viallefond et al. 1992; Wilson & Scoville 1992; Wilson et al. 1997; Churchwell & Goss 1999; Tosaki et al. 2007; Miura et al. 2010; Muraoka et al. 2012; Tachihara et al. 2018), optical (Drissen et al. 1993; Hunter et al. 1996; Yang et al. 1996; González Delgado & Pérez 2000; Tenorio-Tagle et al. 2000; Bruhweiler et al. 2003; Maíz-Apellániz et al. 2004; Relaño & Kennicutt 2009), and infrared (Eldridge & Relaño 2011; Fariña et al. 2012; Martínez-Galarza et al. 2012). According to these earlier studies, NGC 604 contains more than 200 young (3–5 Myr) O-type stars associated with a bright Hα nebula, which seems to be composed of multiple shells, extending up to a radius of 200–400 pc. In addition, the effect of the stellar feedback on the neighboring molecular gas is often discussed. Considering that a huge amount of molecular gas still remains in the close vicinity of NGC 604, which is different from the condition of 30 Dor, NGC 604 is a unique target to investigate both the triggering mechanism of star formation and the feedback from young clusters.

In this paper, we present the results of ALMA observations with an angular resolution of $0\rlap{.}{''}44 \times 0\rlap{.}{''}27$ (corresponding to 1.8 pc × 1.1 pc at the distance of M33) toward the GMC associated with NGC 604 (hereafter, NGC 604-GMC). We also performed high angular resolution ALMA observations toward two other GMCs in M33, GMC-16 and GMC-8, cataloged by Miura et al. (2012), which are in different evolutionary stages from the NGC 604-GMC. The detailed results of GMC-16 are already reported by Tokuda et al. (2020) and those of GMC-8 will be reported in a forthcoming paper (H. Kondo et al. 2020, in preparation).

The structure of this paper is as follows. In Section 2, we describe the ALMA observations and data reduction. Then, we reveal the internal molecular structure of the GMC and its kinematics based on the moment maps of $CO(J = 2 - 1)$ lines, and also present the new finding of 1.3 mm continuum sources as sites of ongoing star formation in Section 3. In Section 4, we first discuss the possible triggering mechanism of high-mass star formation in the NGC 604-GMC, and then we investigate the formation processes of the observed molecular structures and those of dense clumps and high-mass stars at the 1.3 mm continuum sources. In particular, we discuss the role of the galactic-scale gas dynamics in high-mass star formation within parsec-scale molecular clouds.

2. Observations and Data Reduction

ALMA Cycle 6 observations toward NGC 604-GMC were carried out in Band 6 (211–275 GHz) with the main array 12 m antennas and the Atacama Compact Array 7 m antennas between 2017 October and 2018 October. The target field
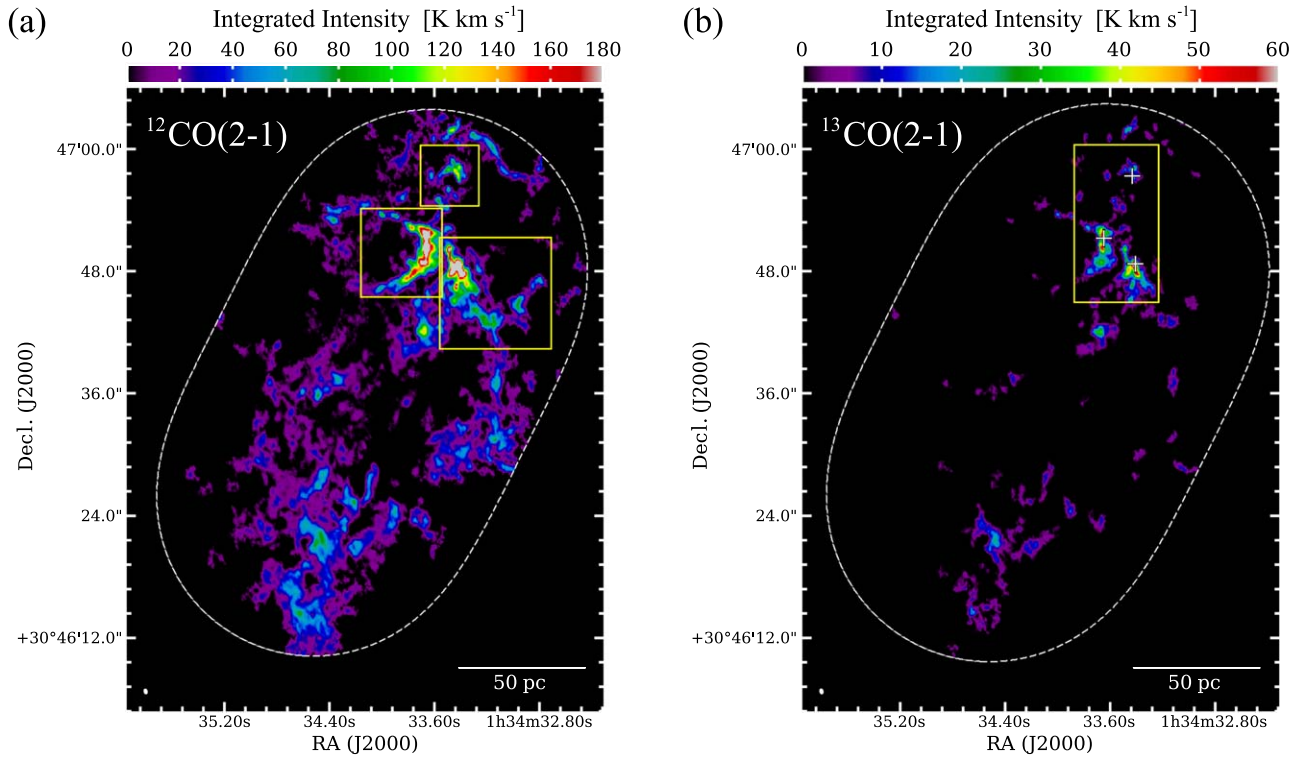
Figure 2. (a) Integrated intensity map in $^{12}CO(J = 2 - 1)$ emission of NGC 604. The dashed white line indicates the field of view of the ALMA observations. The three rectangles indicate individual molecular shells which are magnified and shown in Figure 5. The synthesized beam is shown in the lower left corner. (b) Integrated intensity map in $^{13}CO(J = 2 - 1)$ emission. The rectangle indicates the high molecular gas density region where 1.3 mm continuum emission (crosses) is detected (see Figure 4).

was composed of three adjacent pointings, which could cover most of the NGC 604-GMC, as shown in Figure 1(a).

The target molecular lines were $^{12}CO(J = 2 - 1)$, $^{13}CO(J = 2 - 1)$, and $C^{18}O(J = 2 - 1)$. The bandwidths of the correlator settings were 117.19 MHz with 1920 channels for the ^{12}CO line and 960 channels for ^{13}CO and $C^{18}O$ lines. In addition, we used two spectral windows for the 1.3 mm continuum observations with an aggregate bandwidth of 3750 MHz with a channel width of 0.98 MHz.

We briefly summarize the imaging parameters and resultant data qualities. The detailed processes of data reduction are the same as Tokuda et al. (2020). We used the `tclean` task with the `multi-scale` deconvolver (Kepley et al. 2020), which is imprinted in the Common Astronomy Software Application (CASA) package (McMullin et al. 2007). The weighting scheme of `tclean` was "Briggs" with a robust parameter of 0.5. We combined the 12 m and 7 m array data with the `feathering` task. The beam size of CO data is $0\rlap{.}''44 \times 0\rlap{.}''27$, and the rms noise level is $\sim$1.1 K at a velocity resolution of $\sim$0.2 km s^{-1}. The beam size and the sensitivity of 1.3 mm continuum are $0\rlap{.}''41 \times 0\rlap{.}''25$ and 0.019 mJy beam^{-1}, respectively.

We evaluated the missing flux of the ^{12}CO emission by comparing the single-dish data obtained by the IRAM 30 m telescope (Druard et al. 2014). The flux loss is not significant, not more than $\sim$30% in the 12 m+7 m array data at the northern CO peak (Figure 1), whereas the southern side has a $\sim$50% missing flux. We thus combined the ALMA and the IRAM data using the `feathering` technique. Note that the ALMA program did not include the Total Power array observations. We consider that the 12 m+7 m data of ^{13}CO, $C^{18}O$, and 1.3 mm have no significant missing flux because the

spatial distributions of such dense gas tracers are intrinsically more compact than that of ^{12}CO.

3. Results

3.1. Molecular Gas Properties in ^{12}CO and ^{13}CO

Figure 2 shows the zeroth moment (i.e., integrated intensity) maps in $^{12}CO(J = 2 - 1)$ and $^{13}CO(J = 2 - 1)$ emission. Although the previous single-dish studies only revealed the two local peaks of the GMC (see Figure 1(a)), the new $^{12}CO(J = 2 - 1)$ map clearly depicts complicated molecular gas structures over the observed field. This is the first parsec-scale GMC view at the vicinity of a supergiant H II region in external galaxy disks. We can see several shell- or arc-like CO structures in the northern field, and there exists a lot of molecular filaments with a length of 5–20 pc elongated toward various directions and small (typically less than 10 pc) clumps in the southern field. The $^{13}CO(J = 2 - 1)$ map shows fewer extended distributions compared with that of ^{12}CO, demonstrating that this molecule traces moderately dense gas whose density is $\gtrsim 10^3$ cm^{-3}. The strong $^{13}CO(J = 2 - 1)$ emission is mainly observed in the northern field, in particular, along molecular shells seen in ^{12}CO.

We estimated the H$_2$ gas mass traced by each molecule. We applied the X_{CO} factor, 4×10^{20} cm^{-2} (K km s^{-1})$^{-1}$ (Druard et al. 2014), and a CO(J = 2 - 1)/CO(J = 1 - 0) intensity ratio of 0.85 toward the H II regions (the ratio in the Orion-KL region reported by Nishimura et al. 2015). The total gas mass traced by the ^{12}CO line ($M_{^{12}CO}$) is $\sim 3 \times 10^6 M_\odot$, which is consistent with the single-dish measurements (Gratier et al. 2012). The local thermodynamic equilibrium approximation was applied to estimate the total mass from the ^{13}CO
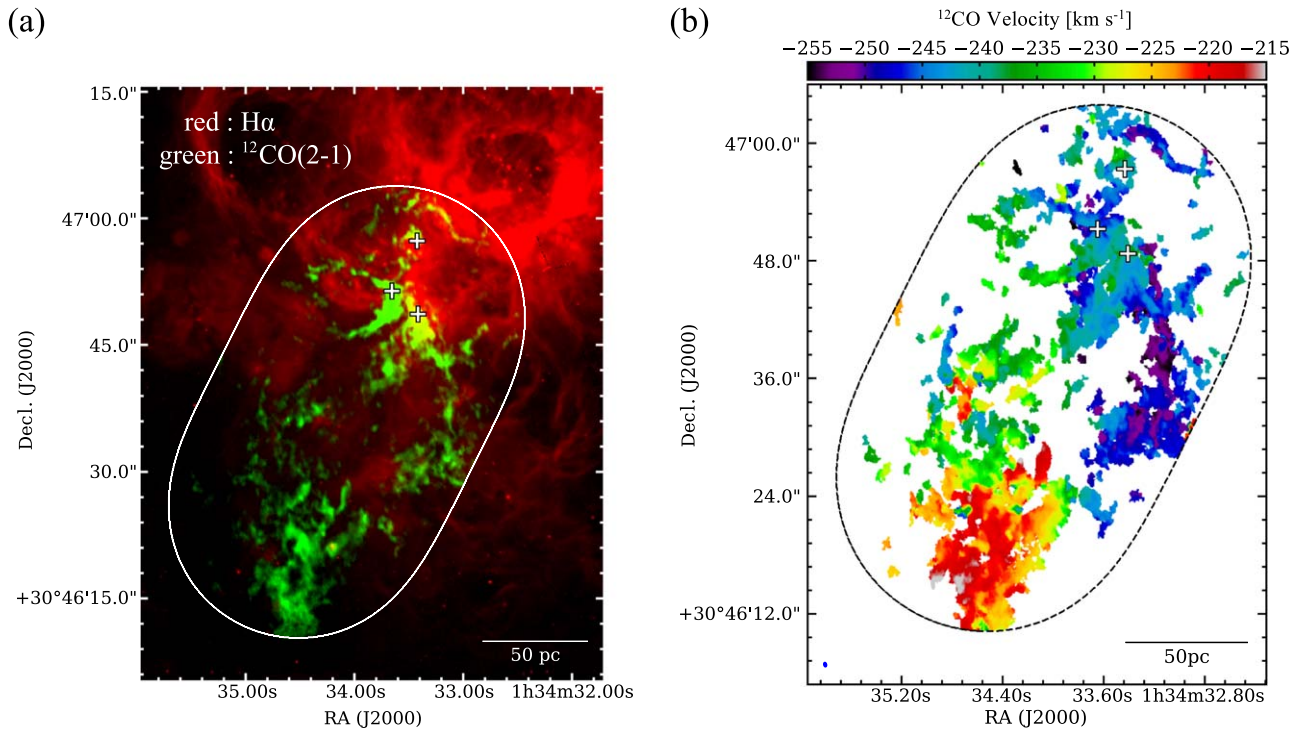
Figure 3. (a) Two-color composite image (green: $^{12}CO(J = 2 - 1)$ intensity by ALMA, red: Hα by HST) of NGC 604. The white line indicates the field of view of the ALMA observations. The crosses are the same as those in Figure 2(b). (b) Velocity field measured in $^{12}CO(J = 2 - 1)$ emission of NGC 604. The synthesized beam is shown in the lower left corner.

observations ($M_{^{13}CO}$) using the excitation temperature of ^{12}CO derived from the peak brightness temperature of the ^{12}CO line and assuming the relative molecular abundance ($[H_2]/[^{13}CO]$) of 1.4×10^6 (see the justification by Tokuda et al. 2020). The resultant $M_{^{13}CO}$ is calculated to be $\sim 3 \times 10^5 M_{\odot}$, and thus the mass ratio ($M_{^{13}CO}/M_{^{12}CO}$) is $\sim 10\%$.

Figure 3(a) shows two-color maps of the ALMA $^{12}CO(J = 2 - 1)$ integrated intensity (green) and the Hα luminosity (red) obtained with the Wide Field and Planetary Camera 2 on the HST, which clearly demonstrates that some molecular shells are associated with H II regions. This suggests that the H II regions affect the neighboring molecular gas; in other words, the feedback should be considered to discuss the structures and physical properties of the molecular shells. We found that the peak temperature of $^{12}CO(J = 2 - 1)$ emission exceeds 40 K at the CO peak in molecular shells. This is presumably due to the heating by UV radiation from high-mass stars within the H II regions.

Figure 3(b) shows the first moment map (i.e., velocity field) in $^{12}CO(J = 2 - 1)$ emission over the observed field. We can see the difference in the representative CO velocities between northern side (-250 to -240 km s^{-1}) and southern side (-230 to -220 km s^{-1}) in the GMC. Such a velocity difference has been already reported by earlier studies (e.g., Miura et al. 2010; Muraoka et al. 2012; Druard et al. 2014). In particular, Tachihara et al. (2018) provided an important clue to understand this velocity difference; they found that the H I clouds in NGC 604 are composed of two velocity components separated by 20 km s^{-1}. The red component corresponds to the "ordinary" velocity expected from the overall rotation of the M33 disk, while the blue component is considered to be infalling H I gas from the eastern side of the GMC (see Figure 1(b)). Note that Tachihara et al. (2018) used the velocity-shifted H I spectra in their analyses in order to

compensate the velocity gradient due to the inclination and galaxy rotation of M33, and thus the two H I velocity components are centered at -185 km s^{-1} and -165 km s^{-1}, respectively. We confirmed that the original H I velocity components in NGC 604 are centered at ~ -250 km s^{-1} and ~ -230 km s^{-1}, which are almost coincident with the two velocity components observed in our ALMA CO data. Since the representative CO velocity in the northern side of NGC 604 corresponds to the blue component, the infalling H I gas likely affects the properties of the molecular gas and the onset of star formation in NGC 604. This will be discussed in Section 4.

3.2. 1.3 mm Continuum and $C^{18}O$ Emission

We found three 1.3 mm continuum sources (MMSs) in the northern part of the observed field as shown in Figure 4. The ID number of the MMSs is assigned according to the 1.3 mm continuum flux, MMS-1, MMS-2, and MMS-3 (see Table 1). The three sources have bright mid-infrared (MIR) emission and they were categorized as massive young stellar object candidates whose enclosed stellar mass is a few $\times 10^3 M_{\odot}$ (Martínez-Galarza et al. 2012). MMS-1, MMS-2, and MMS-3 correspond to Src 1, Src 4, and Src 2 in their catalog, respectively. In addition, two of the three MMSs have counterparts at centimeter wavelength. Churchwell & Goss (1999) reported the 8.4 GHz (3.6 cm) continuum map of NGC 604 at an angular resolution of $2''$ (8 pc), and found six 8.4 GHz components. Their components A and B are coincident with the positions of our MMS-2 and MMS-1, respectively. Since the 8.4 GHz continuum corresponds to the free–free emission from ionized gas, which implies the existence of high-mass stars, the observed MMSs in NGC 604 are considered to be high-mass star-forming regions embedded in dust. Note that the counterpart of MMS-3 is not
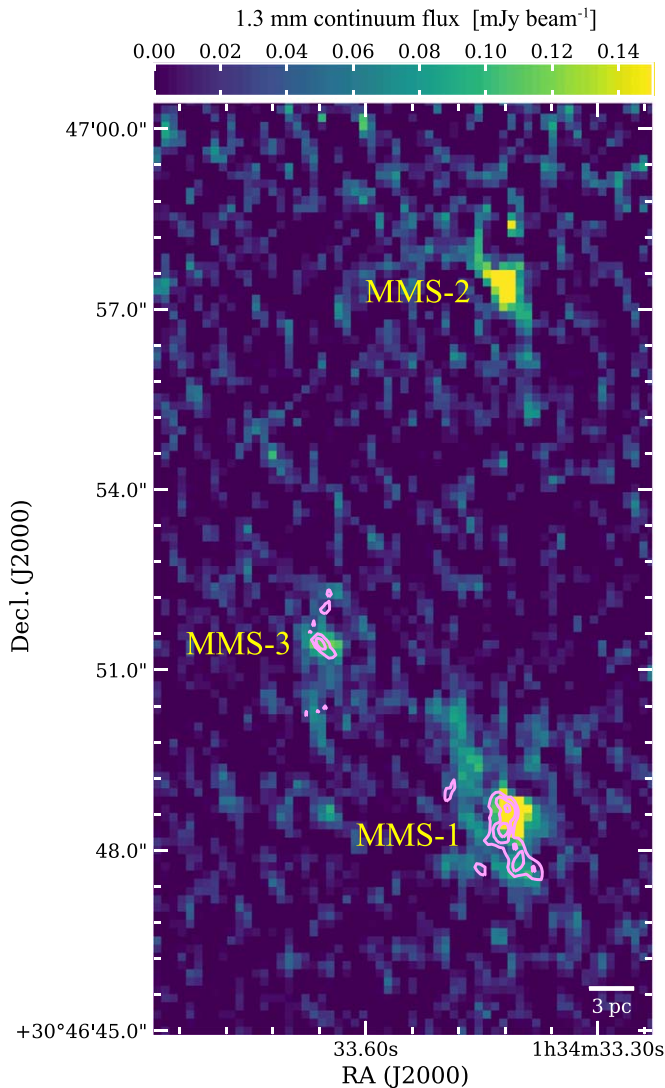
Figure 4. Maps of 1.3 mm continuum flux (color) and the integrated intensity in $C^{18}O(J = 2 - 1)$ emission (contour) of NGC 604. The contour levels are 3, 6, and 9σ, where $1\sigma = 0.53$ K km s^{-1}. Three continuum sources are significantly detected.

identified as an individual component in the 8.4 GHz continuum map. This is presumably due to the insufficient angular resolution of the 8.4 GHz map.

We found a difference in the detection of $C^{18}O(J = 2 - 1)$ emission among these MMSs. Remarkable $C^{18}O(J = 2 - 1)$ emission with peak temperature of 1 K is observed at MMS-1, whereas we found no $C^{18}O(J = 2 - 1)$ emission at MMS-2. We detected moderate $C^{18}O(J = 2 - 1)$ emission whose peak temperature is 0.6 K at MMS-3. Considering that the MMSs are sites of ongoing high-mass star formation, such a difference in the detection of $C^{18}O(J = 2 - 1)$ emission likely reflects different evolutionary stages of star formation (see Section 4.2).

4. Discussion

4.1. Triggering Mechanism of Star Formation

Figure 5 shows the distribution of molecular gas traced by $^{12}CO(J = 2 - 1)$ emission around each MMS in the NGC 604-GMC. Every MMS exists within shell-like molecular structures although the radii of molecular shells are

different from each other. In contrast to this, other cloud peaks in ^{12}CO and ^{13}CO (Figure 2) do not show such remarkable molecular structures and also have neither $C^{18}O$ nor 1.3 mm emission tracing dense clumps. These facts indicate that the molecular clouds associated with the MMSs have experienced a specific compression event to form the massive/dense clumps.

There are some mechanisms which can form such molecular shells and/or trigger high-mass star formation. Energy inputs from supernovae are a possible candidate. Supernovae can supply an enormous amount of mechanical energy to the surrounding ISM, which is enough to form the molecular shell, whereas no supernova is found within the three molecular shells (e.g., Garofali et al. 2017; Long et al. 2018). The role of H II regions containing O-type stars is also important. For example, strong UV radiation from O-type stars ionizes the surrounding neutral ISM. Since the ionized region radially spreads, a molecular shell is finally formed. However, the ionization of neutral ISM cannot induce the high-mass star formation because it does not compress the surrounding molecular gas. Instead, expansion of the H II region is a potential candidate. Earlier studies (e.g., Elmegreen 1998 and references therein) suggest that the high pressure of H II regions yields direct compression of preexisting clouds and globules ("globule squeezing"), and/or gas that is accumulated into a dense ridge or shell (i.e., the edge of H II regions), and then the cloud collapses gravitationally into dense cores ("collect and collapse").

In Figure 6(a), we examined the individual comparison between spatial distributions of the molecular shell and the H II region around each MMS. We found that all the molecular shells with MMSs are associated with H II regions. In particular, the molecular shell with MMS-2 seems clear along the edges of its internal H II regions. A similar spatial correspondence can be observed for the molecular shell with MMS-1 although the Hα emission along the western part of the shell is relatively weak. The molecular shell with MMS-3 is slightly away from the edge of the adjacent H II region (in particular, the southern part of the shell). In order to investigate whether the expansion of an individual H II region within each molecular shell triggers high-mass star formation at the MMSs, we examine the velocity structures based on the $^{12}CO(J = 2 - 1)$ position–velocity (PV) diagrams, which are perpendicularly extracted to the possible expansion direction of each H II region, as shown in Figures 6(b) and (c). Torii et al. (2015) qualitatively described that PV diagrams in CO show an elliptical shape if the expanding motion of the H II region compresses the surrounding molecular materials (see their Figure 8). The PV diagrams observed around the three MMSs show a nearly constant velocity field centered at the systemic velocity of $\sim$240 km s^{-1} with somewhat local fluctuations, rather than a large-scale elliptical shape throughout the clouds. Note that we found a small elliptical shape at the vicinity of MMS-1 in the PV diagram (Figure 6(b)). This implies that the expansion of the ionized gas can *locally* sweep the molecular material, yet it may not contribute to the entire structure formation in their parental molecular clouds and to the high-mass star formation at MMS-1. This hypothesis is consistent with a numerical study by Shima et al. (2017), suggesting that stellar feedbacks do not primarily affect gas structures in the molecular clouds. Thus, we concluded that the expansion of

Table 1
Properties of 1.3 mm Continuum Sources

Source ID	R.A.	Decl.	Size (pc)	F_{peak} (mJy beam^{-1})	F_ν (mJy)	ΔV (km s^{-1})	M_{vir} ($M_\odot$)	$n(H_2)$ (cm^{-3})	M_{total}^{MMS} ($M_\odot$)
(1)	(2)	(3)	(4)	(5)	(6)	(7)	(8)	(9)	(10)
MMS-1	01 34 33.42	30 46 48.59	2.9×1.9	0.37	1.2	6.0	1.8×10^4	1.8×10^4	4.5×10^4
MMS-2	01 34 33.42	30 46 57.31	3.2×1.6	0.29	0.9	6.0	1.7×10^4	1.9×10^4	3.3×10^4
MMS-3	01 34 33.63	30 46 51.38	3.2×2.2	0.12	0.5	5.7	1.8×10^4	1.3×10^4	1.9×10^4

Note. (1) ID number of each MMS. (2)–(3) Position of the peak 1.3 mm flux at each MMS in equatorial coordinates (J2000). (4) Source size (FWHM) derived from 2D elliptical Gaussian fitting. (5) Peak 1.3 mm flux. (6) Total 1.3 mm flux. (7) Velocity width (FWHM) of C^{18}O($J = 2 - 1$) emission of MMS-1 and MMS-3 and ^{13}CO($J = 2 - 1$) emission of MMS-2. (8) Virial mass calculated from the following relation, $M_{vir} = 210\Delta V^2 R$, where R is the geometric mean of the source size. (9) Number density of molecular gas derived from the source size and the virial mass. (10) Mass derived from the total continuum flux, assuming a dust temperature of 22 K (Tabatabaei et al. 2014), a gas-to-dust ratio of 300 (Relaño et al. 2018), and $\kappa_{1.3\,mm}$ of 1 cm^2 g^{-1} for protostellar envelopes (Ossenkopf & Henning 1994).

H II regions is not a likely trigger of high-mass star formation at MMSs in the NGC 604-GMC.

An alternative potential mechanism which can trigger high-mass star formation is cloud–cloud collision. In the next subsection, we investigate whether the cloud–cloud collision can explain the high-mass star formation at each MMS.

4.2. Formation Processes of the Massive Clumps as Promising Formation Sites of High-mass Stars

As shown in Table 1, the MMSs show massive and dense characteristics. The Spitzer observations identified bright MIR sources toward the MMSs (Section 3.2), indicating that the high-mass star formation is actively ongoing (see also Martínez-Galarza et al. 2012). Since the three MMSs (and also their parental molecular clouds) are spatially separated as shown in Figures 2 and 4, they likely have different origins. Thus, we discuss possible formation mechanisms of each dense clump, MMS-1, MMS-2, and MMS-3, individually.

4.2.1. MMS-1

Figure 7(a) shows the maps of the ^{13}CO($J = 2 - 1$) integrated intensity and 1.3 mm continuum emission around MMS-1. The peak position of the ^{13}CO($J = 2 - 1$) intensity is almost coincident with not only MMS-1 but also the strong Hα spot (see Figure 6(a)), the bright MIR source, and the local peak of 8.4 GHz continuum emission (see Section 3.2). Furthermore, we found that multiple molecular filaments extend from the peak, showing the parasol-like structure. The first moment map (Figure 7(b)) shows velocity differences among each filament; the eastern filament (No. 1) has a central velocity of ~ -240 km s^{-1}, but those of the other two filaments (Nos. 2 and 3) are ~ -243 km s^{-1}. The typical length and mass of the filaments are ~ 15 pc and $\sim 3 \times 10^3\,M_\odot$, respectively. These characteristics are similar to those in molecular filaments associated with 30–40 $M_\odot$ protostars in the N159 GMC (Fukui et al. 2015; Saigo et al. 2017), which is one of the most active star-forming regions in the LMC (e.g., Fukui et al. 2008; Minamidani et al. 2008; Chen et al. 2010). Fukui et al. (2015) and Saigo et al. (2017) suggested that filament–filament collisions promoted the high-mass star formation at the intersections.

However, instead of the filament–filament collision scenario, Fukui et al. (2019) and Tokuda et al. (2019) claimed a large-scale colliding flow scenario in N159 based on higher-resolution studies. Their ^{13}CO($J = 2 - 1$) observations found the parasol-like structures composed of more than a few tens of filaments, and also found high-mass protostars at the pivots.

Observations toward the Galactic high-mass star-forming regions often identify such complex filamentary configurations, called a "hub filament" (e.g., Myers 2009; Peretto et al. 2013; Williams et al. 2018). Numerical simulations by Inoue et al. (2018) suggested that the formation of such a complex/massive filamentary structure, whose line mass exceeds $\sim 1000\,M_\odot$, occurs after a collision between small and large clouds. Fukui et al. (2019) and Tokuda et al. (2019) concluded that a large-scale colliding flow is more likely to explain the observed filamentary clouds and the star formation activities therein. One of the promising candidates of the origin of the large-scale flow is the past tidal interaction between the LMC and the Small Magellanic Cloud (Fukui et al. 2017; Tsuge et al. 2019).

We apply such a mechanism to MMS-1 in NGC 604. In the case of MMS-1, molecular filaments (i.e., ribs of a parasol) extend southward from the CO peak. This suggests that a small cloud from the south side collided with a preexisting large cloud. If we assume the trailing spiral arm and gas streaming to be based on the density-wave theory, the flowing direction of the gas clouds is considered to be from south to north (i.e., upstream to downstream of the spiral arm). The speed of the interstellar gas originated from the galactic rotation at NGC 604, ~ 3.5 kpc from the galactic center (Gratier et al. 2012), is ~ 100 km s^{-1} (Corbelli et al. 2014). If we subtract a pattern speed, Ω_p, of ~ 25 km s^{-1} kpc^{-1} (Newton 1980), the possible colliding gas velocity is likely more than ~ 10 km s^{-1}, which is consistent with the numerical setup by Inoue et al. (2018). Note that such a large velocity difference of more than ~ 10 km s^{-1} is *not* observed around MMS-1 as shown in Figure 7(b). This is because the initial collision velocity is decelerated at the shock front and/or the direction of collision is perpendicular to the line of sight. The latter effect is especially serious in the case of external galaxies whose inclination is close to face-on.

In summary, we suggest that the hub filament at MMS-1 was formed by the collision between a small cloud flowing from upstream of the spiral arm and a preexisting large cloud within the molecular shell, and then high-mass star formation occurred. Tokuda et al. (2020) also found a similar hub–filamentary complex in GMC-16, which is radially extended toward the upstream side of the galactic rotation. Considering the fact that the strong C^{18}O($J = 2 - 1$) emission tracing dense molecular gas is observed at MMS-1, this high-mass star formation seems to be in an earlier stage.

Note that we suppose that the molecular shell with MMS-1 was formed by the ionization due to UV radiation from O-type stars within the internal H II region because the molecular shell is along the edge of the H II region although the Hα emission
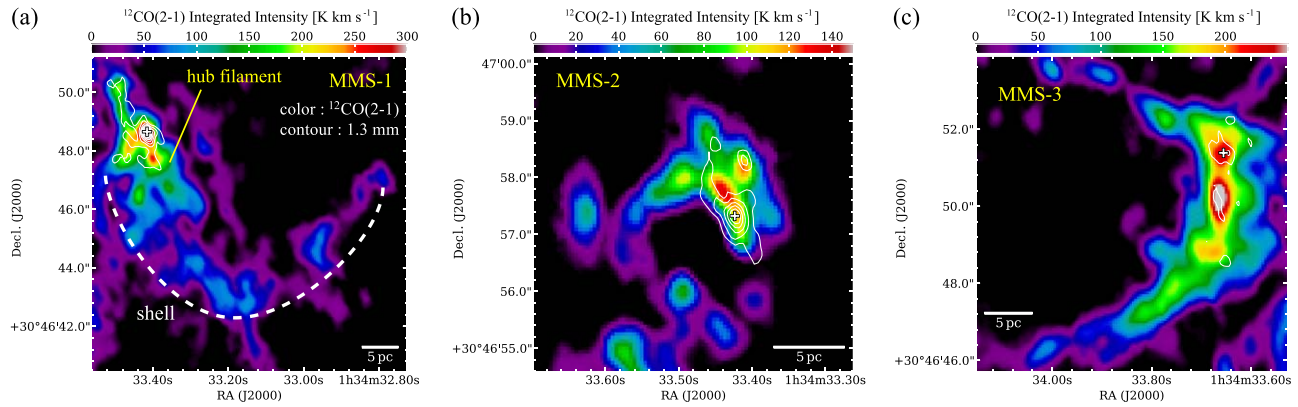
Figure 5. Maps of 1.3 mm continuum flux (contour) superposed on integrated intensity maps in $^{12}CO(J = 2 - 1)$ emission (color) around each molecular shell containing MMSs. The contour levels are 3, 6, 9, 12, 15, 18, and 21σ, where $1\sigma = 0.02$ mJy beam^{-1}. The crosses are the same as those in Figure 2(b).

along the western part of the shell is relatively weak (Figure 6(a)).

4.2.2. MMS-2 and MMS-3

As shown in Figures 5(b) and 6(a), MMS-2 exists at the overlapping region between the strong $H\alpha$ spot of a small H II region and the surrounding molecular shell. Such a spatial distribution of each emission is quite similar to that of the Galactic H II region RCW 120, which is classified as a *Spitzer* bubble (Churchwell et al. 2006). According to Torii et al. (2015), the triggering mechanism of high-mass star formation in RCW 120 can be explained by a cloud–cloud collision. Based on the theoretical model introduced by Habe & Ohta (1992), they suggested that the exciting O-type star in RCW 120 was formed by a collision between the present two (small and large) clouds at a collision velocity of $\sim$30 km s^{-1}. In this scenario, the molecular shell can be interpreted as the cavity created in the larger cloud by the collision. However, an alternative interpretation is also suggested; for example, Zavagno et al. (2020) claimed that they revealed the structure of the dense photodissociation region associated with RCW 120 and evidence for the compression of the internal H II region. Thus, the formation mechanism of such a ring/ shell structure and that of subsequent high-mass stars are just in discussion even for the MW sources.

In the case of MMS-2, the observed velocity structure in $^{12}CO(J = 2 - 1)$ suggests that the molecular shell is not likely due to the expansion of H II regions as described in the previous subsection. We thus discuss whether the cloud–cloud collision model can explain the observed molecular shell and high-mass star formation at MMS-2-like RCW 120 (Torii et al. 2015). MMS-2 exists on the western side of the molecular shell. If the cloud–cloud collision model similar to RCW 120 is applied to MMS-2, a small cloud flowed from east to west and finally collided with a large cloud. This flowing direction of the small cloud is consistent with the infalling H I gas suggested by Tachihara et al. (2018) (see Section 3.1). Therefore, the cloud–cloud collision seems to be an acceptable model to explain the observed feature of MMS-2.

We found no $C^{18}O(J = 2 - 1)$ emission at MMS-2 as described in Section 3.2. However, the molecular gas density at MMS-2 exceeds 10^4 cm^{-3} (see Table 1), which is comparable to those at MMS-1 and MMS-3 where the significant $C^{18}O(J = 2 - 1)$ emission is detected. This is likely explained by the selective photodissociation of $C^{18}O$ molecules due to the

far-UV radiation as in the cases of the Galactic molecular clouds (e.g., Lada et al. 1994; Buckle et al. 2012; Shimajiri et al. 2014). We thus consider that the high-mass star formation at MMS-2 is in a later stage than the other MMSs.

We then explore whether the cloud–cloud collision model can explain MMS-3 and its surrounding molecular shell. Since MMS-3 exists in the western side of the molecular shell, similar to the case of MMS-2, the infalling H I gas likely contributes to the formation of the molecular shell through the cloud–cloud collision. In fact, we found a possible gas colliding signature on the PV diagram (Figure 6(b)); there exists a high-velocity component, called the V-shaped feature (e.g., Fukui et al. 2018), centered at the position of MMS-3. However, the $H\alpha$ emission is relatively weak inside the molecular shell with MMS-3 compared to that with MMS-2. According to the extinction map of the NGC 604-GMC (e.g., Maíz-Apellániz et al. 2004; Relaño & Kennicutt 2009), extinction at MMS-3 is comparable to that at MMS-2. Thus, the weak $H\alpha$ emission at MMS-3 is not caused by the strong extinction by dust, but presumably due to the inactive high-mass star formation.

A similar case has been observed toward the Galactic source; Higuchi et al. (2014) found a molecular shell possibly formed by a cloud–cloud collision at G0.253+0.016 (G0.25 cloud) in the Galactic center, whereas the high-mass star formation is inactive inside the shell. They concluded that the G0.25 cloud is in the very early stage of star formation, triggered by the cloud–cloud collision. We thus suppose that the high-mass star formation at MMS-3 is in an earlier stage, which is consistent with the existence of dense molecular gas traced by the moderate $C^{18}O(J = 2 - 1)$ emission.

4.2.3. A Possible Origin of Different Morphologies in the Molecular Clouds around the MMSs

The parental clouds of MMS-2 and MMS-3 show shell-like structures, whereas that of MMS-1 is a hub–filament structure composed of at least three components. The former is similar to collision products by the Habe & Ohta model (Habe & Ohta 1992; Takahira et al. 2014; Shima et al. 2018). The latter can be reproduced by the Inoue et al. (2018) model as discussed in Section 4.2.1. This discrepancy is presumably due to the differences in the initial conditions of the cloud–cloud collisions between the two models. In the Habe & Ohta model, they simulated a collision between two spherical clouds, while Inoue et al. (2018) treated a collision between a small spherical
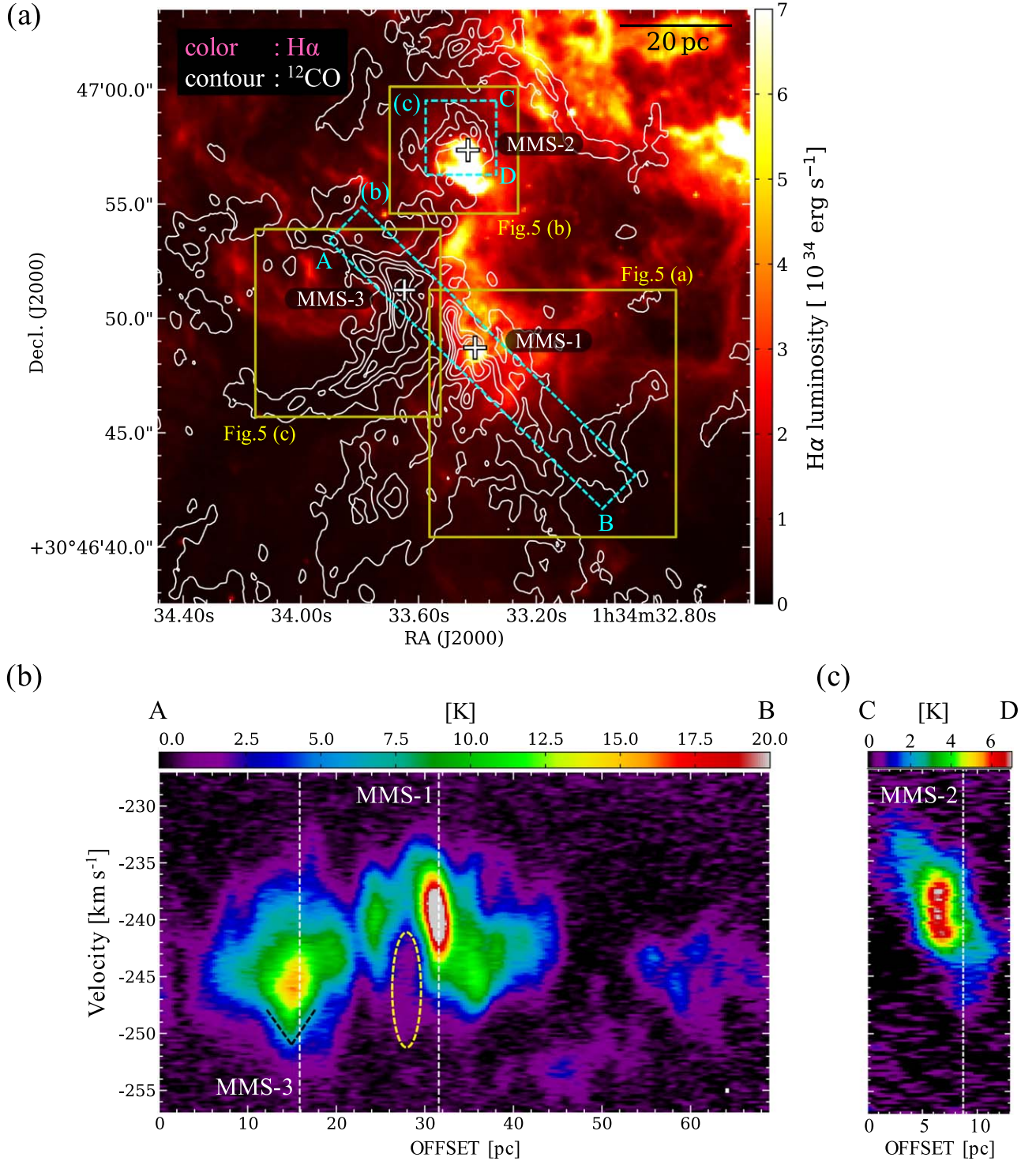
(a)

(b)

(c)

Figure 6. (a) Integrated intensity map in ^{12}CO($J = 2 - 1$) emission (contour) superposed on the map of Hα emission (color) around each molecular shell containing MMSs. The contour levels are 10, 30, 60, 90, 120, 150, 180, and 210 K km s^{-1}. The three yellow rectangles are the same as in Figure 2(a). The crosses are the same as those in Figure 2(b). The dashed rectangles show the regions where the position–velocity diagrams are extracted. (b), (c) ^{12}CO($J = 2 - 1$) position–velocity diagrams extracted from the position A to B and from C to D shown in (a). The white vertical lines denote the positions of the MMSs. The yellow ellipse indicates the possible expansion of the ionized gas which may locally sweep the molecular material. The black dashed line indicates the high-velocity CO component (the V-shaped feature), suggesting a possible gas colliding signature. The spatial and velocity resolutions are shown in the lower right corner of (b).

cloud and a large cloud surface filling a part of the numerical cubic box.

Magnetic field properties may be also important because dense filamentary structures are efficiently formed when the magnetic field orientation is perpendicular to the collision direction (Inoue et al. 2018). Recently, Sakre et al. (2021) investigated the effect of magnetic field on the Habe & Ohta model. When the collision direction is perpendicular to the strong (4 μG) magnetic field, the collision product is close to our detected "hub" composed of three linear-shaped filaments rather than a shell-like structure, which is formed in the parallel magnetic field case. From an observational perspective, a radio-
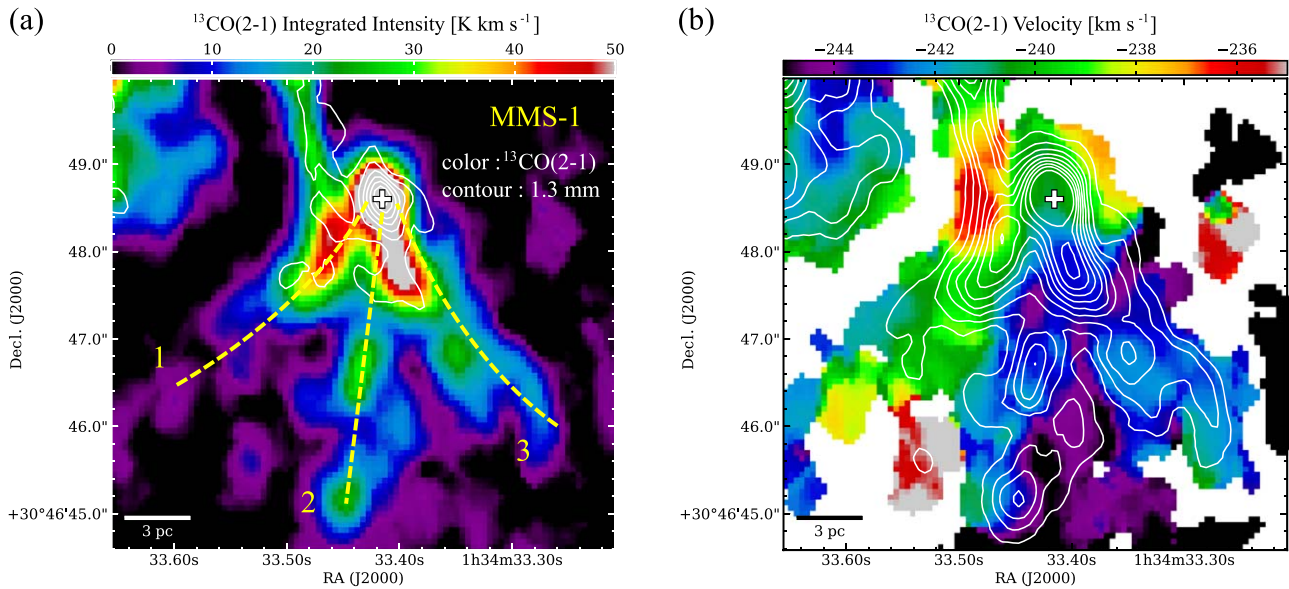
Figure 7. (a) Map of 1.3 mm continuum flux (contour) superposed on integrated intensity map in $^{13}CO(J = 2 - 1)$ emission (color) around MMS-1. The contour levels are the same as those in Figure 5(a). The dashed lines indicate individual molecular filaments. (b) Maps of velocity field (color) and integrated intensity (contour) in $^{13}CO(J = 2 - 1)$ emission around MMS-1. The contour levels are 6, 12, 18, 24, 30, 36, 42, 48, and 56 K km s^{-1}. The cross in each panel indicates the peak position of 1.3 mm continuum flux.

continuum polarization study by Tabatabaei et al. (2008) revealed that the magnetic field orientation toward the NGC 604-GMC is in the east–west direction. This might explain the observed molecular gas structures around MMSs; i.e., the cloud–cloud collision in the north–south direction (i.e., perpendicular to the magnetic field) at MMS-1 formed the hub–filamentary shape, whereas those in the east–west direction (i.e., parallel to the magnetic field) at MMS-2 and MMS-3 produced shell-like features. However, the actual magnetic field properties toward the molecular phase are still unknown because the available CO polarization measurement with a much higher spatial resolution (∼15 pc) toward M33 by Li & Henning (2011) intrinsically contains the 90° ambiguity of the Goldreich–Kylafis effect. Future high-resolution/high-sensitivity polarization observations combining CO and thermal dust emission will complementarily constrain the magnetic field properties in the NGC 604-GMC.

4.3. Star Formation Scenario in NGC 604

For NGC 604, a scenario of sequential star formation has been discussed. In particular, Tosaki et al. (2007) found a high CO(J = 3 − 2)/CO(J = 1 − 0) ratio gas arc along the bright Hα nebula, and suggested that the high-ratio gas arc revealed the presence of warm and dense molecular gas layers, which were compressed by stellar wind and/or supernovae from the central star cluster of NGC 604. They concluded that the arc-like structure of the high-ratio gas is the site of second-generation star formation triggered by first-generation star formation (i.e., the central star cluster).

The location of the high-ratio gas arc roughly corresponds to the northern field of the ALMA observations, where strong $^{12}CO(J = 2 - 1)$ and $^{13}CO(J = 2 - 1)$ emission and 1.3 mm continuum emission are observed (see Figures 2 and 4). Thus, the three MMSs are considered to be at least a part of the second-generation star formation suggested by Tosaki et al. (2007). However, the triggering mechanism of the high-mass star formation at the MMSs is not likely the feedback from the

central star cluster and/or H II regions, but cloud–cloud collisions are instead, as discussed in Section 4.2. We suppose that there is little relationship between the ongoing high-mass star formation at MMSs and the central star cluster of NGC 604. Instead, the galactic-scale gas dynamics play an important role in the ongoing high-mass star formation in NGC 604.

We compare our results with numerical simulations of isolated spiral galaxies. Dobbs et al. (2018) found that a model with higher feedback best reproduced the M33-like spiral structure in the gas. The higher feedback generally makes neighboring molecular clouds smaller. In fact, small clouds whose typical size is less than 10 pc are observed in the southern part of the NGC 604-GMC (see Figure 2). Such a small cloud may produce the observed hub filament at MMS-1 through the cloud–cloud collision. Dobbs et al. (2015) suggested that moderate- and long-lived clouds experience one or more cloud–cloud collisions within their lifetime.

In Figure 8, we summarize the schematic view of our proposed star formation scenario in NGC 604. Tachihara et al. (2018) found two H I components with a velocity separation of ∼20 km s^{-1} in NGC 604, and suggested that the blueshifted velocity components triggered the first-generation star formation. Even after the drastic cluster formation, the converging gas is still energetic enough to propagate the star formation activities southward. The colliding flow remnant triggered the formation of MMS-2, which is likely the most evolved one among the three MMSs, and subsequently formed MMS-3 and its surrounding molecular structure. Note that the parental molecular gas of MMS-1 possibly originates from the preexisting cloud in the southern side of NGC 604; i.e., its origin is *not* converging H I gas flow, but likely the galactic rotation. The role of the galactic rotation in the compression of the molecular material has been already pointed out by Tosaki et al. (2007).

The NGC 604 complex contains one of the most mass-concentrated GMCs in M33, and the molecular gas structures show well-developed filaments, which have dense clumps
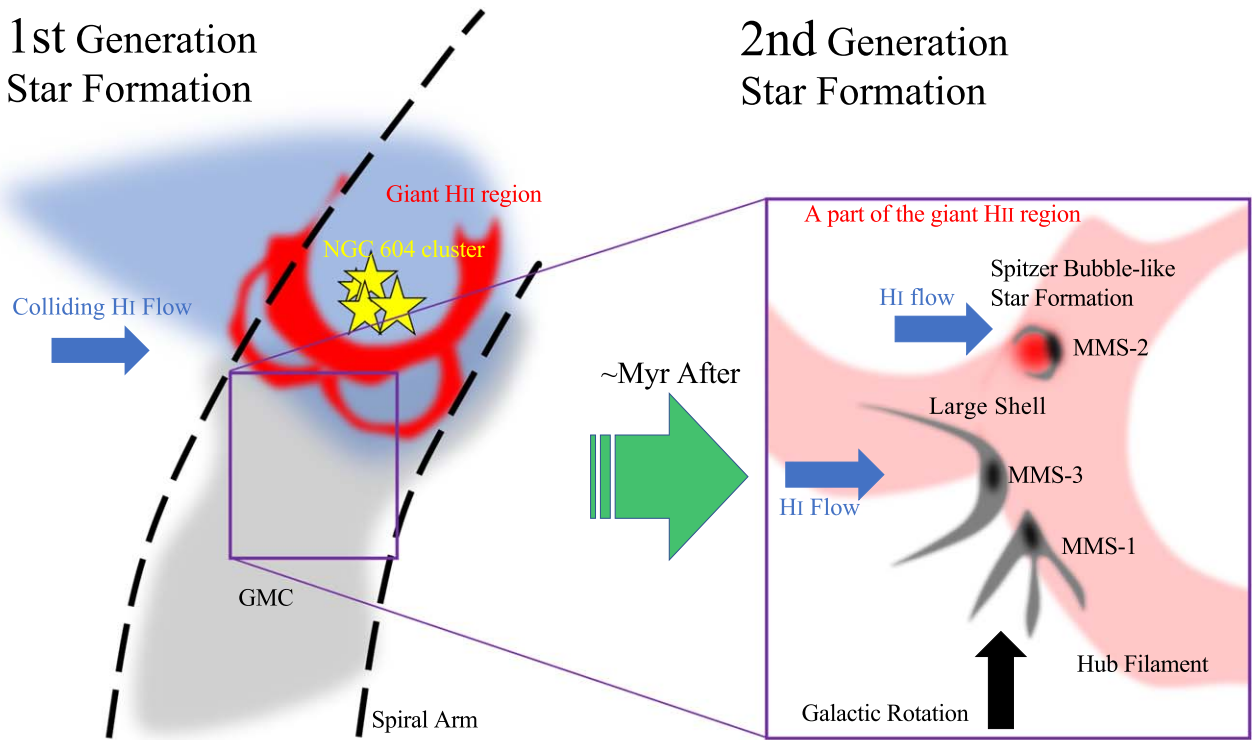
Figure 8. Schematic view of the star formation process in NGC 604 motivated by the ALMA observations. Note that the colliding H I gas was proposed by Tachihara et al. (2018).

identified at the millimeter wavelength. In contrast to this, GMC-16 shows filamentary clouds with a length of $\sim$50 pc along with the spiral arm (Tokuda et al. 2020) and GMC-8 shows an extended round-shaped structure without any remarkable dense filaments/clumps (H. Kondo et al. 2020, in preparation) although the two GMCs have a comparable molecular mass ($\sim$$10^6 \, M_\odot$) to the NGC 604-GMC. The resolved GMC structures may provide us crucial hints to understand their formation history. In the case of NGC 604, we suggest that galactic-scale gas flows from at least two directions work to build up the largest high-mass star-forming complex in the Local Group of galaxies.

5. Summary

We have performed ALMA observations in ^{12}CO($J = 2 - 1$), ^{13}CO($J = 2 - 1$), and C^{18}O($J = 2 - 1$) lines and 1.3 mm continuum emission toward a GMC associated with the giant H II region NGC 604 at an angular resolution of $0\rlap{.}{''}44 \times 0\rlap{.}{''}27$ (1.8 pc $\times$ 1.1 pc). The summary of this work is as follows:

1. The molecular gas distributions in the ^{12}CO and ^{13}CO lines are highly structured, i.e., composed of a lot of molecular filaments, arcs, and shells whose lengths are 5–20 pc, indicating the evolved nature of the GMC. The total H$_2$ gas masses estimated from the ^{12}CO and ^{13}CO data are $\sim$3 $\times$ $10^6 \, M_\odot$ and $\sim$3 $\times$ $10^5 \, M_\odot$, respectively.
2. We have identified three 1.3 mm continuum sources (MMS-1, MMS-2, and MMS-3) with a gas mass of $\sim$$10^4 \, M_\odot$ at the edges of the hub filament and shells. We detected C^{18}O emission at MMS-1 and MMS-3 but not in MMS-2. This discrepancy is presumably due to their different evolutionary stages. The presence of the massive/dense clumps strongly indicates that the high-

mass star formation is still ongoing even after the formation of the first-generation cluster embedded in the giant H II region.
3. We revealed that the ^{12}CO peak temperature at the northern molecular complex is as high as $\sim$40 K, and some of the molecular shells are along the edge of H II regions. These observational facts indicate that the giant H II regions contribute to the heating and the ionization of surrounding ISM. However, the CO velocity structures indicate that the expanding motion of H II regions does not promote the compression of the molecular material to trigger the second-generation star formation. Alternatively, multiple cloud–cloud collisions induced by an external H I gas flow and the galactic rotation may explain the formation of the molecular shells and the hub filament associated with dense clumps as the birth sites of high-mass stars.

Software: CASA (v5.4.0; McMullin et al. 2007), Astropy (Astropy Collaboration et al. 2018), APLpy (v1.1.1; Robitaille & Bressert 2012).

ORCID iDs

Kazuyuki Muraoka ⓘ https://orcid.org/0000-0002-3373-6538
Kazuki Tokuda ⓘ https://orcid.org/0000-0002-2062-1600
Atsushi Nishimura ⓘ https://orcid.org/0000-0003-0732-2937
Rie E. Miura ⓘ https://orcid.org/0000-0001-8187-7856
Nario Kuno ⓘ https://orcid.org/0000-0002-1234-8229
Sarolta Zahorecz ⓘ https://orcid.org/0000-0001-6149-1278
Kisetsu Tsuge ⓘ https://orcid.org/0000-0002-2794-4840
Hidetoshi Sano ⓘ https://orcid.org/0000-0003-2062-5692
Shinji Fujita ⓘ https://orcid.org/0000-0002-6375-7065
Toshikazu Onishi ⓘ https://orcid.org/0000-0001-7826-3837
Kazuya Saigo ⓘ https://orcid.org/0000-0003-1549-6435
Kengo Tachihara ⓘ https://orcid.org/0000-0002-1411-5410
Akiko Kawamura ⓘ https://orcid.org/0000-0001-7813-0380

References

Astropy Collaboration, Price-Whelan, A. M., Sipőcz, B. M., et al. 2018, AJ, 156, 123
Blitz, L., Fukui, Y., Kawamura, A., et al. 2007, Protostars and Planets V (Tucson, AZ: Univ. Arizona Press), 81
Bruhweiler, F. C., Miskey, C. L., & Smith Neubig, M. 2003, AJ, 125, 3082
Buckle, J. V., Davis, C. J., di Francesco, J., et al. 2012, MNRAS, 422, 521
Chen, C.-H. R., Indebetouw, R., Chu, Y.-H., et al. 2010, ApJ, 721, 1206
Churchwell, E., & Goss, W. M. 1999, ApJ, 514, 188
Churchwell, E., Povich, M. S., Allen, D., et al. 2006, ApJ, 649, 759
Corbelli, E., Braine, J., Bandiera, R., et al. 2017, A&A, 601, A146
Corbelli, E., & Salucci, P. 2000, MNRAS, 311, 441
Corbelli, E., Thilker, D., Zibetti, S., et al. 2014, A&A, 572, A23
Dobbs, C., & Baba, J. 2014, PASA, 31, e035
Dobbs, C. L., Pettitt, A. R., Corbelli, E., et al. 2018, MNRAS, 478, 3793
Dobbs, C. L., Pringle, J. E., & Duarte-Cabral, A. 2015, MNRAS, 446, 3608
Drissen, L., Moffat, A. F. J., & Shara, M. M. 1993, AJ, 105, 1400
Druard, C., Braine, J., Schuster, K. F., et al. 2014, A&A, 567, A118
Eldridge, J. J., & Relaño, M. 2011, MNRAS, 411, 235
Elmegreen, B. G. 1998, in ASP Conf. Series 148, Origins, ed. C. E. Woodward et al. (San Francisco, CA: ASP), 150
Engargiola, G., Plambeck, R. L., Rosolowsky, E., et al. 2003, ApJS, 149, 343
Fariña, C., Bosch, G. L., & Barbá, R. H. 2012, AJ, 143, 43
Freedman, W. L., Madore, B. F., Gibson, B. K., et al. 2001, ApJ, 553, 47
Fujimoto, M. 1968, in IAU Symp. 29, Non-stable Phenomena in Galaxies (Yerevan: Academy of Sciences of Armenian SSR), 453
Fukui, Y., Harada, R., Tokuda, K., et al. 2015, ApJL, 807, L4
Fukui, Y., & Kawamura, A. 2010, ARA&A, 48, 547
Fukui, Y., Kawamura, A., Minamidani, T., et al. 2008, ApJS, 178, 56
Fukui, Y., Tokuda, K., Saigo, K., et al. 2019, ApJ, 886, 14
Fukui, Y., Torii, K., Hattori, Y., et al. 2018, ApJ, 859, 166
Fukui, Y., Tsuge, K., Sano, H., et al. 2017, PASJ, 69, L5
Garofali, K., Williams, B. F., Plucinsky, P. P., et al. 2017, MNRAS, 472, 308
Goldsmith, P. F., Heyer, M., Narayanan, G., et al. 2008, ApJ, 680, 428
González Delgado, R. M., & Pérez, E. 2000, MNRAS, 317, 64
Gratier, P., Braine, J., Rodriguez-Fernandez, N. J., et al. 2010, A&A, 522, A3
Gratier, P., Braine, J., Rodriguez-Fernandez, N. J., et al. 2012, A&A, 542, A108

Habe, A., & Ohta, K. 1992, PASJ, 44, 203
Hacar, A., Tafalla, M., Kauffmann, J., et al. 2013, A&A, 554, A55
Heyer, M., & Dame, T. M. 2015, ARA&A, 53, 583
Heyer, M. H., Corbelli, E., Schneider, S. E., et al. 2004, ApJ, 602, 723
Higuchi, A. E., Chibueze, J. O., Habe, A., et al. 2014, AJ, 147, 141
Hopkins, P. F., Quataert, E., & Murray, N. 2012, MNRAS, 421, 3488
Hunter, D. A., Baum, W. A., O'Neil, E. J., et al. 1996, ApJ, 456, 174
Inoue, T., Hennebelle, P., Fukui, Y., et al. 2018, PASJ, 70, S53
Kepley, A. A., Tsutsumi, T., Brogan, C. L., et al. 2020, PASP, 132, 024505
Lada, C. J., Lada, E. A., Clemens, D. P., et al. 1994, ApJ, 429, 694
Li, H.-B., & Henning, T. 2011, Natur, 479, 499
Lin, C. C., & Shu, F. H. 1964, ApJ, 140, 646
Long, K. S., Blair, W. P., Milisavljevic, D., et al. 2018, ApJ, 855, 140
Maíz-Apellániz, J., Pérez, E., & Mas-Hesse, J. M. 2004, AJ, 128, 1196
Martínez-Galarza, J. R., Hunter, D., Groves, B., et al. 2012, ApJ, 761, 3
McKee, C. F., & Ostriker, E. C. 2007, ARA&A, 45, 565
McMullin, J. P., Waters, B., Schiebel, D., et al. 2007, in ASP Conf. Series 376, Astronomical Data Analysis Software and Systems XVI, ed. R. A. Shaw et al. (San Francisco, CA: ASP), 127
Minamidani, T., Mizuno, N., Mizuno, Y., et al. 2008, ApJS, 175, 485
Miura, R., Okumura, S. K., Tosaki, T., et al. 2010, ApJ, 724, 1120
Miura, R. E., Kohno, K., Tosaki, T., et al. 2012, ApJ, 761, 37
Miura, R. E., Kohno, K., Tosaki, T., et al. 2014, ApJ, 788, 167
Mizuno, A., Onishi, T., Yonekura, Y., et al. 1995, ApJL, 445, L161
Muraoka, K., Tosaki, T., Miura, R., et al. 2012, PASJ, 64, 3
Myers, P. C. 2009, ApJ, 700, 1609
Newton, K. 1980, MNRAS, 190, 689
Nishimura, A., Tokuda, K., Kimura, K., et al. 2015, ApJS, 216, 18
Onishi, T., Mizuno, A., Kawamura, A., et al. 1996, ApJ, 465, 815
Onodera, S., Kuno, N., Tosaki, T., et al. 2010, ApJL, 722, L127
Ossenkopf, V., & Henning, T. 1994, A&A, 291, 943
Peretto, N., Fuller, G. A., Duarte-Cabral, A., et al. 2013, A&A, 555, A112
Relaño, M., De Looze, I., Kennicutt, R. C., et al. 2018, A&A, 613, A43
Relaño, M., & Kennicutt, R. C. 2009, ApJ, 699, 1125
Roberts, W. W. 1969, ApJ, 158, 123
Robitaille, T., & Bressert, E. 2012, APLpy: Astronomical Plotting Library in Python, Astrophysics Source Code Library, ascl:1208.017
Rosolowsky, E., Keto, E., Matsushita, S., et al. 2007, ApJ, 661, 830
Saigo, K., Onishi, T., Nayak, O., et al. 2017, ApJ, 835, 108
Sakre, N., Habe, A., Pettitt, A. R., et al. 2021, PASJ, in press, doi:10.1093/pasj/psaa059
Sano, H., Tsuge, K., Tokuda, K., et al. 2021, PASJ, in press, doi:10.1093/pasj/psaa045
Shima, K., Tasker, E. J., Federrath, C., et al. 2018, PASJ, 70, S54
Shima, K., Tasker, E. J., & Habe, A. 2017, MNRAS, 467, 512
Shimajiri, Y., Kitamura, Y., Saito, M., et al. 2014, A&A, 564, A68
Shu, F. H., Milione, V., & Roberts, W. W. 1973, ApJ, 183, 819
Tabatabaei, F. S., Braine, J., Xilouris, E. M., et al. 2014, A&A, 561, A95
Tabatabaei, F. S., Krause, M., Fletcher, A., et al. 2008, A&A, 490, 1005
Tachihara, K., Gratier, P., Sano, H., et al. 2018, PASJ, 70, S52
Takahira, K., Tasker, E. J., & Habe, A. 2014, ApJ, 792, 63
Tenorio-Tagle, G., Muñoz-Tuñón, C., Pérez, E., et al. 2000, ApJ, 541, 720
Tokuda, K., Fukui, Y., Harada, R., et al. 2019, ApJ, 886, 15
Tokuda, K., Muraoka, K., Kondo, H., et al. 2020, ApJ, 896, 36
Torii, K., Hasegawa, K., Hattori, Y., et al. 2015, ApJ, 806, 7
Tosaki, T., Kuno, N., Onodera, S. M., et al. 2011, PASJ, 63, 1171
Tosaki, T., Miura, R., Sawada, T., et al. 2007, ApJL, 664, L27
Tsuge, K., Sano, H., Tachihara, K., et al. 2019, ApJ, 871, 44
Viallefond, F., Boulanger, F., Cox, P., et al. 1992, A&A, 265, 437
Williams, G. M., Peretto, N., Avison, A., et al. 2018, A&A, 613, A11
Wilson, C. D., & Scoville, N. 1992, ApJ, 385, 512
Wilson, C. D., Walker, C. E., & Thornley, M. D. 1997, ApJ, 483, 210
Yang, H., Chu, Y.-H., Skillman, E. D., et al. 1996, AJ, 112, 146
Zavagno, A., André, P., Schuller, F., et al. 2020, A&A, 638, A7